RSC Advances

PAPER

View Article Online
View Journal | View Issue

Cite this: *RSC Adv.*, 2023, **13**, 7372

Simultaneous precipitation and discharge plasma processing for one-step synthesis of α-Fe_2O_3–Fe_3O_4/graphene visible light magnetically separable photocatalysts†

Nguyen Long Tuyen,[ab] Tran Quoc Toan,*[c] Nguyen Ba Hung,[d] Pham Quoc Trieu,[a] Nguyen Ngoc Dinh,[a] Danh Bich Do,[e] Dang Van Thanh[fg] and Van-Truong Nguyen*[h]

Received 29th October 2022
Accepted 21st February 2023

DOI: 10.1039/d2ra06844c

rsc.li/rsc-advances

A novel facile combination of precipitation and plasma discharge reaction is successfully employed for one-step synthesis of an α-Fe_2O_3–Fe_3O_4 graphene nanocomposite (GFs). The co-existence and anchoring of hematite (α-Fe_2O_3) and magnetite (Fe_3O_4) nanoparticles onto a graphene sheet in the as synthesized GFs were verified by results of XRD, Raman, SEM, TEM, and XPS. HRTEM characterization was used for confirming the bonding between α-Fe_2O_3/Fe_3O_4 nanoparticles and the graphene sheet. Consequently, GFs shows superior photodegrading performance towards methylene blue (MB), compared to individual α-Fe_2O_3/Fe_3O_4 nanoparticles, as a result of band gap narrowing and the electron–hole pair recombination rate reducing. Moreover, GFs allows a good possibility of separating and recycling under an external-magnetic field, suggesting potential in visible-light-promoted photocatalytic applications.

1. Introduction

In recent years, magnetic metal oxides such as Fe_3O_4 and Fe_2O_3 have drawn increased attention, which is attributed to their high saturation magnetization and wide light absorption area.[1,2] Due to these properties, magnetic materials can be used for magnetic separation and photocatalysis. However, there are bottle necks remaining such as a fast electron–hole recombination rate and poor conductivity which have limited them for application in many sectors.[3–5] Therefore, many approaches to improve Fe_xO_y photocatalytic ability under visible light irradiation have been offered such as creating defects in the material structure,[6] doping with metal or non-metal atoms[7] and/or coupling with carbon-based materials.[8–10] The synergistic effects of two different materials coexist which enlarge their properties compared to those of individual components.[11,12] Among them, graphene/metal oxide nanocomposites (GMOs) have been intensively studied as photocatalysts for removing pollutants from water owing to the improving of the photocatalytic activity and enhancing of the stability and suppressing the photo-corrosion.[13–15] For example, a core-satellite and dumbbell-like Fe_3O_4@C–Ag composites were reported by Wang *et al.* using a solvothermal process. The metal–carbon interfaces were contributed in the high catalytic recyclable performance for the degradation of RhB.[16] In another research, the Fe_3O_4/rGO was prepared by a co-precipitation and reduction process.[17] This composite revealed 3.7 times higher adsorption capacity for RhB and 30 times faster adsorption rates than those of activated carbon. For further improvement, ternary materials based on iron oxide were also explored using various methods to take advantage of the superior properties of the individual materials.[10,18] For example, B. Saiphaneendra and his group reported the rGO supported (α-Fe_2O_3 and Fe_3O_4) nanocomposite material which revealed the good absorption and high reusability of the composites due to the synergistic of hematite and magnetite nanoparticles on graphene sheet.[10] Typically, a lot of methods is designed to prepare the above-mentioned nanocomposite, such as solution mixing,[19] sol–gel,[20,21] hydrothermal/solvothermal method,[22] self-assembly,[23,24] *etc.* However, these aforementioned methods still have obvious drawbacks such as complicated procedure, long-time reaction,

[a]*VNU University of Science, 334 Nguyen Trai Str., Thanh Xuan Dist., Hanoi, Vietnam*
[b]*Hung Vuong University, Nong Trang, Viet Tri City, Phu Tho, Vietnam*
[c]*Faculty of Chemistry, Thai Nguyen University of Education, 20 Luong Ngoc Quyen, Thai Nguyen, Vietnam*
[d]*Vietnam Military Medical University, 160 Phung Hung, Ha Dong, Hanoi, Vietnam*
[e]*Faculty of Physics, Hanoi National University of Education, 136 Xuan Thuy, Cau Giay, 100000, Hanoi, Viet Nam*
[f]*TNU-University of Medicine and Pharmacy, 284 Luong Ngoc Quyen, Thai Nguyen, Vietnam*
[g]*Faculty of Environmental Sciences, University of Science, Vietnam National University, 334 Nguyen Trai Road, Ha Noi City 100000, Hanoi, Vietnam*
[h]*Faculty of Fundamental and Applied Science, Thai Nguyen University of Technology, 666, 3/2 Street, Tich Luong Ward, Thai Nguyen, Vietnam. E-mail: vtnguyen@tnut.edu.vn*

† Electronic supplementary information (ESI) available. See DOI: https://doi.org/10.1039/d2ra06844c

high temperature, and high-pressure requirements. For example, the sol–gel or solvothermal/hydrothermal routes typically require complicated conditions and high temperatures. Sol–gel approach has the time limitations. In addition, the Hummers' method required to prepare GO (rGO), a precursor material, often causes secondary pollution due to the involvement of redox agents or toxic solvents. Hence, the development of an one-step method for preparing GMOs at room temperature and under mild conditions is currently a technical challenge.

In this study, we propose a novel coupling precipitation reaction and discharge plasma processing for one-step synthesis of an α-Fe_2O_3–Fe_3O_4/graphene nanocomposite (GFs). This synthesis approach enables the *in situ* formation and decoration of α-Fe_2O_3–Fe_3O_4 onto the surface of the electrochemically exfoliated graphene sheets under an atmospheric environment. The as-synthesized GFs exhibited improved in visible-light absorption and charge separation through DRS, PL, EIS and methylene blue photodegradation of GFs under visible light irradiation with highly efficient magnetic separation. This simple approach opens the suitable and economically viable production of visible-light driven and magnetically recyclable nanocomposites for the various applications.

2. Materials and methods

2.1. Materials

All chemicals used are analytical chemicals: iron(III) sulfate hydrate ($Fe_2(SO_4)_3 \cdot xH_2O$), iron(II) sulfate heptahydrate ($FeSO_4 \cdot 7H_2O$), sodium hydroxide (NaOH), sodium sulfate (Na_2SO_4), methylene blue (MB) dyes, high purity graphite rod (99.999%, 150 mm length and radius of 6 mm) was purchased from Sigma-Aldrich.

2.2. Fabrication of iron oxides

$Fe_2(SO_4)_3 \cdot xH_2O$ (7.99 g) and $FeSO_4 \cdot 7H_2O$ (2.78 g) were dissolved in 150 mL of distilled water, followed by magnetic stirring at 60 °C for 30 minutes. The mixture was then slowly dripped into a beaker containing 200 mL NaOH 0.5 M, which was ultrasonically vibrated for 2 hours. After the reaction time, the reddish brown resulting mixture was filtered, and the solid product was washed several times with distilled water and dried at 80 °C for 24 hours. This material is identified as Fe_xO_y (iron oxide), and it is stored and used in further experiments.

2.3. Fabrication of graphene/iron oxide composites

Fig. 1 illustrates the graphene/iron oxide composite fabrication model. Accordingly, the entire two electrode electrochemical system includes a cathodic graphite rod and anodic platinum foils set into a flask of electrolyte solution which is placed in an ultrasonic vibrating tank. In the meantime, the mixture of $Fe_2(SO_4)_3 \cdot xH_2O$ (7.99 g) and $FeSO_4 \cdot 7H_2O$ (2.78 g) was dissolved in 150 mL of distilled water. We maintained this mixture solution at 60 °C for 30 min under a slight stirring level of 100 RPM. First, the sharpened graphite rod is located about 1 mm to 2 mm above the electrolyte solution level. The anode platinum foil was embedded at 5 cm depth in the electrolyte solution. The using electrolyte solution is 200 mL NaOH 0.5 M. Secondly, a direct current (DC) source with a voltage of 120 V was applied to two electrodes. The sharpened tip of the graphite rod was descended gradually into electrolytes which induced the plasma zone at the electrolyte touching position under the high asymmetric electric field. Then, the mixture solution of Fe^{3+} and Fe^{2+} was slowly added to the electrolyte solution at a drop rate of 2 mL min^{-1} when the plasma discharge and ultrasonic vibration were performing. The composites materials of GFs were simultaneously generated by the flow of electrons from the negative electrode to be discharged directly and the solution plasma conditions. This experiment was performed in 75 min. The as-prepared materials were collected by the filtration system using the PVDF membrane with the pore size of 0.2 μm. The resulting powder was washed in distilled water at least 3 times and then dried 24 hours at 80 °C in air. The obtained composite material is denoted as GF and using for further characterization.

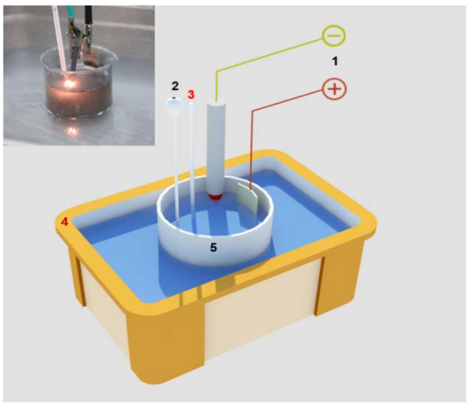

Fig. 1 Illustration of the experimental setup for graphene/iron oxide composites material fabrication.

2.4. Measuring equipment

X-ray diffraction patterns were used to investigate the structural changes of the fabricated samples (D2 PHASER Machine). The morphology of the samples was investigated by a scanning electron microscope (JEOL JSM – 6700F) and a transmission electron microscope (JEM-F200). The covalent and atomic bonds in the material were analyzed by X-ray photoelectron spectroscopy method (09A2 U5-spectroscopy beam line for XPS, Hsinchu, Taiwan). Raman spectroscopy was performed using a Labram HR evolution raman spectrometer (Horiba, Japan). The optical properties of samples were characterized by V770 UV-vis spectrophotometer (Jasco, Japan), Nicolet iS50 FTIR spectrometer (Thermo scientific, American), and Fluorolog-QM fluorescence spectrophotometer (Horiba, Japan). The magnetic properties and saturation magnetization were recorded using a VSM (MicroSence EZ9). Electrochemical impedance spectra (EIS) were conducted using an Autolab workstation PGS 302N assembly with Pt counter electrode, Ag/AgCl electrode, reference electrode, and GF-coated carbon paper working electrode.

The working electrode was fabricated by dripping 100 μL of a mixed solution of GF, carbon black and polyvinylidene difluoride (PVDF) with the ratio 80 : 10 : 10 in *N*-methyl pyrrolidinone solvent at a concentration of 10 mg mL^{-1} on carbon paper substrate (with the surface area of 1 cm^2) then dried at 50 °C for 12 hours. The solution used in the EIS measurements is Na_2SO_4 1 M.

2.5. Photocatalytic experiments

A small amount of methylene blue – MB (3 mg) was dissolved in 150 mL of distilled water to generate a solution with a concentration of 20 ppm. After that an amount of 0.02 g as-prepared materials (Fe_xO_y or GF) was added into the MB solution. Then, the mixture was magnetically stirred for 30 minutes to achieve adsorption–desorption equilibrium. After that, the photocatalytic experiment was performed by illuminating a 400 W xenon lamp coupling with 400 nm UV filter into the mixture solution. A little volume of the reaction mixture (1.5 mL) was collected at every 15 minutes, centrifuged for 10 minutes at 6000 rpm, and analyzed by UV-vis absorption spectra to determine the concentration of MB in solution through absorbance measurements at 664 nm.

3. Results and discussion

3.1. Structural and morphological characterizations

Fig. 2 shows XRD pattern of graphene, Fe_xO_y and GF composite samples, respectively, measured in the 2 theta angle range of 10° to 80°. The evidence diffraction peaks located at 26° reveals the purity of graphene corresponded to (002) plane of graphene structure.[25,26] As compared to the Fe_xO_y pattern, the peaks at 26° reflected the existence of graphene in GF samples. On the other hand, six obvious diffraction peaks in the patterns of both Fe_xO_y and GF samples at 30.1°; 35.5°; 43.1°; 53.5°; 57.05°; 62.7° corresponding to the crystal planes (220); (311); (222); (422); (511) and (440) of Fe_3O_4 structure with lattice constant a = 8.378 Å, b = 8.378 Å, c = 8.378 Å, α = 90°, β = 90° and γ = 90°. The relatively sharp diffraction peaks in the Fe_xO_y and GF samples demonstrate the fine crystallization of Fe_3O_4. However, the α-Fe_2O_3 composition has not been clearly recognized. This may be due to peak overlap between α-Fe_2O_3 and Fe_3O_4, and/or can be assigned to the more sensitivity of Fe_3O_4 than those of α-Fe_2O_3 or probably because of incomplete crystallization of α-Fe_2O_3. This opinion will be confirmed by the further characterization.

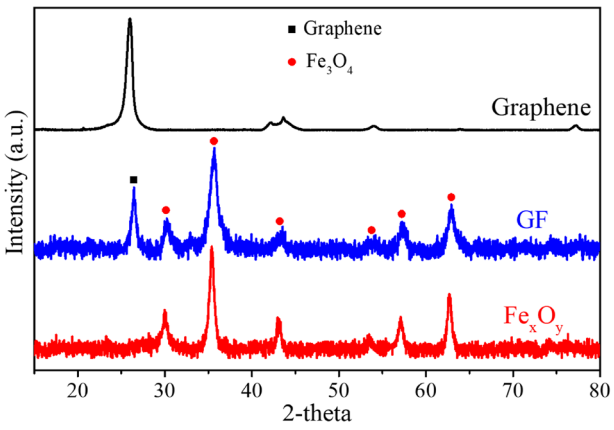

Fig. 2 XRD pattern of graphene, Fe_xO_y and GF composite samples.

Raman spectra can provide additional information on the structural material. Fig. 3(a) displays Raman spectra of graphene, Fe_xO_y, and GF composite samples, respectively. Graphene samples with characteristic peaks at 1352 cm^{-1}, 1567 cm^{-1}, and 2698 cm^{-1} corresponded to the D, G, and 2D bands, respectively.[27] The strong symmetric 2D band peak at 2698 cm^{-1} indicated common vibration of ordered sp^{2-} hybridized carbon atoms by the E_{2g} phonon mode, which revealed the high quality of graphene. Peaks at 211 cm^{-1}, 270 cm^{-1}, and 379 cm^{-1} in the Fe_xO_y sample were assigned to one oscillation mode A_{1g} and two modes E_g of iron oxide, respectively.[28,29] In addition, the appearance of the peak at 215 cm^{-1} and 279 cm^{-1} in the Raman spectra of the GF revealed the coexistence of the Fe_3O_4 in the GF structure[30] (Fig. 3(c)). Moreover, the characteristic peaks for graphene in GF were slightly shifted to 1352 cm^{-1} (D band), 1567 cm^{-1} (G band), and 2652 cm^{-1} (2D band), respectively (Fig. 3(a and b)). Notably, the 2.38 time higher of I_D/I_G intensity ratio (0.31) of GF than that of graphene samples (0.13) related to the increasing of disorder in the carbon network structure of graphene. This result can be attributed to the binding of Fe_xO_y with the graphene. Thus, the coexistence of the Fe_3O_4 and graphene peaks in the Raman result, as well as the previous XRD result, it can be expected that the composites at least two components: Fe_3O_4 and graphene.

Fig. 3(d) depicts the Fourier-transform infrared spectroscopy (FTIR) of graphene, Fe_xO_y, and GF samples, which are measured in the 400–4000 cm^{-1} range. In all three samples, the wide peaks at ~3418 cm^{-1} and 1628 cm^{-1} are attributed to the stretching and bending vibrations O–H of H_2O,[31] respectively; the 2360 cm^{-1} peak is also due to CO_2 binding.[32] For the graphene sample, in addition to the adsorption peak characteristic for the presence of the C=C bond in the sample at 1576 cm^{-1}, the peaks are characteristic of the C–OH bond (1381 cm^{-1}),

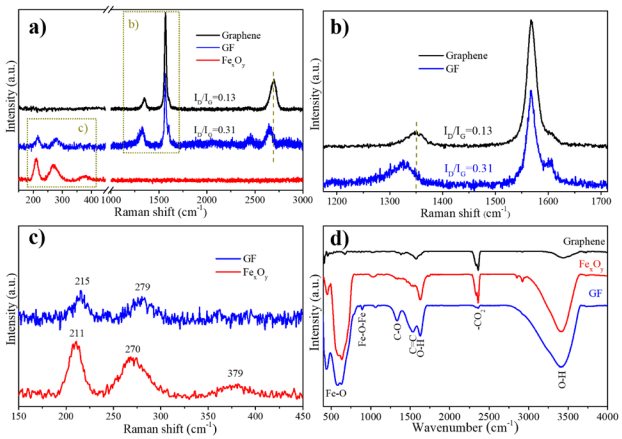

Fig. 3 (a), (b), and (c): Raman spectra of Fe_xO_y, graphene, and GF composite samples; (d) FTIR spectrum of graphene, Fe_xO_y, and GF samples.

carboxyl CO (1419 cm^{-1}), epoxy CO (1219 cm^{-1}) were also found.[33] The peaks at 628 cm^{-1}, 586 cm^{-1}, and 451 cm^{-1} on both the Fe_xO_y and the GF – combinant samples are assigned to the stretching mode of the Fe–O bond, indicating that they both have an iron oxide component. Compared to the Fe_xO_y sample, the GF sample also showed more peaks at 891 cm^{-1}, 1335 cm^{-1}, and 1535 cm^{-1}, corresponding to C=C, C–O, and Fe–O–Fe bridges, respectively. The shift of the C=C peak from 1576 cm^{-1} (graphene) to 1535 cm^{-1} (GF) is attributed to the incorporation of iron oxide into the graphene lattice.

Fig. 4 presents the SEM and TEM images of Fe_xO_y and GF for morphology investigation. The SEM images of Fe_xO_y and GF are shown in Fig. 4(a and b), respectively. The uniform spherical Fe_xO_y nanoparticles tend to agglomerate to form clusters. After a discharge plasma of graphite rod in the Fe^{2+}/Fe^{3+} precursor solution, the graphene nanosheets were decorated by the clusters of Fe_xO_y nanoparticles as displayed in the SEM image of GF sample. Fig. 4(c–f) show the low and high resolution TEM images of the Fe_xO_y and GF samples. The spherical particles observed in both Fe_xO_y and GF samples with size ranging from 5 to 10 nm as shown in Fig. 4(c and d). This result revealed that the morphology and size of Fe_xO_y nanoparticles were maintained under the high energy of the discharge plasma. Furthermore, the uniform Fe_xO_y particles surrounding the ultrathin graphene nanosheets were evidently shown in the TEM image of GF (Fig. 4(d)). In addition, the detail lattice

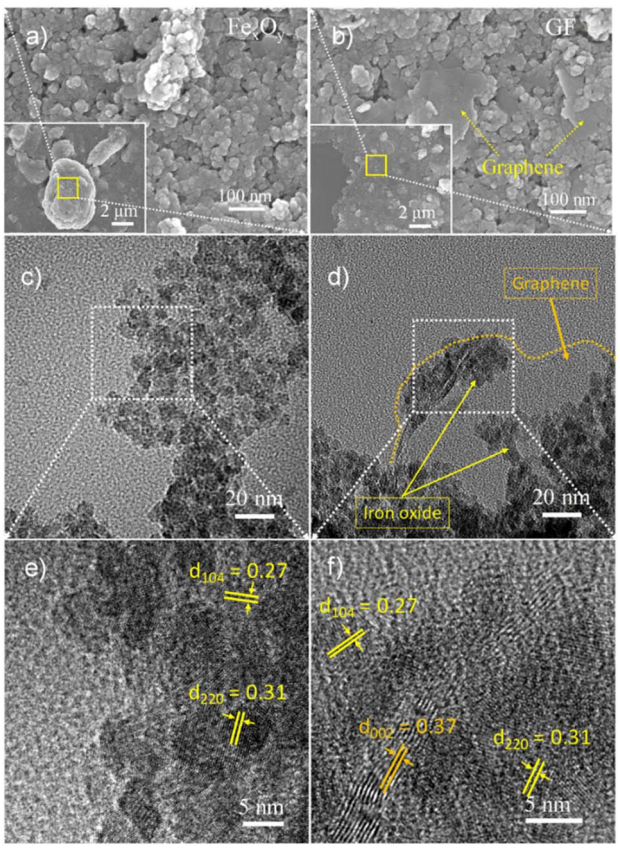

Fig. 4 SEM images of (a) Fe_xO_y, (b) GF; low-magnification TEM images of (c) Fe_xO_y, (d) GF; HRTEM images of (e) Fe_xO_y, (f) GF.

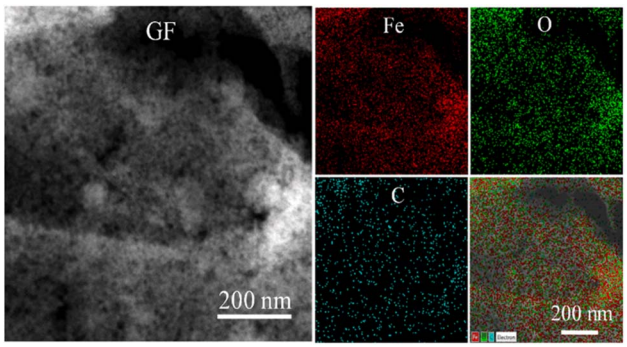

Fig. 5 Dark-field STEM of GF and its corresponding EDS element mapping.

structure of Fe_xO_y and GF were investigated by the HRTEM images as presented in Fig. 4(e and f). From the edges of graphene nanosheets in the Fig. 4(f), the Fast Fourier transform (FFT) was used to determine the layer dispacing of 0.37 nm correspond to (002) lattice plane of graphene nanosheets. This result is larger than that of the theoretical value which attributed to the discharge plasma distorted the weak van der Waals bonding of graphite. Interestingly, the α-Fe_2O_3 ((104) lattice plane) and Fe_3O_4 ((220) lattice plane) structures assigned to the corresponding lattice dispacing of 0.27 and 0.31 nm coexist in both Fe_xO_y and GF samples. This result reveals that our method offers an effective route to build the multipurpose ternary composite of graphene/Fe_xO_y.

Fig. 5 shows the dark-field STEM of GF and its corresponding EDS element mapping. The uniform distribution of Fe in the red color and the O in the green color located on the carbon in the cyan color were confirmed. These results highly agreed with the TEM results of GF.

X-ray photoelectron spectroscopy (XPS) measurement was utilized to further probe the chemical composition of GF. Fig. 6 depicts the XPS spectrum of the GF composite sample. The peaks locate at 55 eV, 284.5 eV, 530 eV, 710 eV, and 723 eV in the survey spectrum of the GF sample correspond to Fe 3p, C 1s, O 1s, and Fe 2p, respectively, indicating the presence of the elements C, O, and Fe (Fig. 6(a)). The O 1s core level XPS spectra

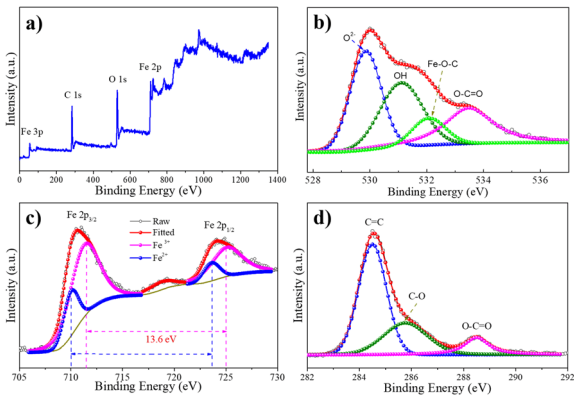

Fig. 6 XPS spectra of the samples: (a) survey, (b) O 1s, (c) Fe 2p, and (d) C 1s.

can be deconvoluted into four peaks by the Gaussian fitting, as displayed in Fig. 6(b). The peaks corresponding to the binding energies of 529.8, 531.1, and 533.5 eV can be ascribed to the O^{2-}, O–H, and O–C=O components, respectively. Moreover, the formation of Fe–O–C bonding can be attributed to the peak at 532.1 eV.[34,35] This result can be interpreted as a demonstration of the bond formation between Fe_xO_y and the graphene plane *via* functional groups on the graphene surface. Therefore, the plasma energy not only provides graphene nanosheets for the composite but also induces the chemical bonding of graphene and Fe_xO_y structure to form the multipurpose ternary composite. In Fig. 6(c), the high resolution core level of Fe 2p spectrum displays a pair of peaks at 710.3 eV and 724.3 eV assigned to Fe $2p_{3/2}$ and Fe $2p_{1/2}$, respectively. With using the split energy of 13.6 eV, the double peaks fitting at 711.4, 725 eV, and 710, 723.6 eV correspond to the core level of Fe^{3+} and Fe^{2+}, respectively.[36,37] This result is highly agreed with the HRTEM analysis. In particular, the elemental ratio of 3.55/1 from XPS results in estimation compared to the ionic precursor ratio of 4/1 for Fe^{3+}/Fe^{2+} highly revealed the controllability of this approach. The XPS C 1s spectrum of the GF sample in Fig. 6(d) was analyzed into three components corresponding to the oxygen-free group C=C sp^2 (284.5 eV), the epoxy group, and the alkoxyl group C–O (285.2 eV) and the carboxylate group O–C=O (288.5 eV).

3.2. Mechanism of material formation

Fig. 7 illustrates the mechanism of the formation of graphene/iron oxide composite material. First, the strong asymmetry electric field between the graphite cathode tip and the electrolyte (liquid electrode) knocks on electrons out of the cathode interfaces. These electrons move under the influence of the strong electric field and then ionizes the air, resulting in plasma formation in the volume between the cathode and the electrolytes. Ions, radicals and photons are mainly generated in the plasma region. The collision of ions and oxidized radicals with not only the graphite electrode but also the electrolyte surface increases the temperature at this region. Meanwhile, the increasing temperature, combined with the intercalation of ions and oxidized radicals into the graphite structure, breaks the weak van der Waals bonding leading to exfoliating graphene sheets from the graphite electrode. In addition, oxygen-containing functional groups may be added in the meantime.

When dripping the solution mixture (Fe^{2+}/Fe^{3+}) in an alkaline medium, Fe^{2+} and Fe^{3+} are converted into $Fe(OH)_2$, $Fe(OH)_3$, and FeOOH. Further reactions form Fe_3O_4 or Fe_2O_3 under plasma conditions as follows.

$$2Fe^{3+} + Fe^{2+} + 8OH^- \rightarrow Fe_3O_4 + 8H_2O \quad (1)$$

$$FeOOH \rightarrow Fe_2O_3 + H_2O \quad (2)$$

The graphite layers were being peeled off to form graphene at the same time as the iron salt solution mixture was added to an alkaline environment. The shear force caused by the ultrasonic wave continues to separate the graphene layers while also assisting the Fe_xO_y nanoparticles in rapidly depositing and evenly dispersing the Fe_xO_y nanoparticles on the graphene film. Under the influence of plasma, the reaction process can combine iron oxide with functional groups on rGO to create graphene/Fe_2O_3/Fe_3O_4 composite material.

3.3. Magnetic properties

Fig. 8 shows the magnetization hysteresis loop of the Fe_xO_y, GF composite, and graphene sample measured in the magnetic field from −10 000 to 10 000 Oersted at room temperature. The iron oxide and GF samples have saturated magnetizations of 55.1 emu g^{-1} and 48.8 emu g^{-1}, respectively. The reduction of saturation magnetization in GF samples comes from the non-magnetic phase of graphene. Interestingly, GF exhibited good magnetic recovery from solution by applying an external magnetic field, as shown in the inset inside Fig. 8. The material was carefully re-collected by a recycling process (see ESI† for additional details). These results showed that GF could be an excellent candidate for practical wastewater treatment.

3.4. Photocatalytic activity

The recombination of charge carriers has a significant influence on the material's photocatalytic activity. Photoluminescence (PL) spectroscopy was used to investigate the charge carrier transfer and electron–hole recombination processes. In addition, electrochemical impedance spectroscopy (EIS) is a useful method for the charge-carrying properties of materials

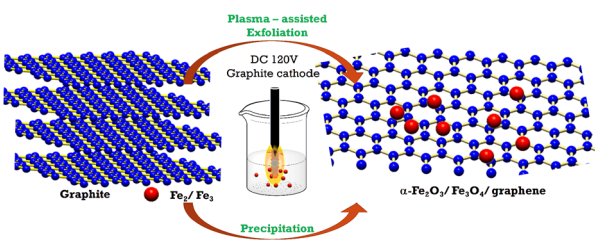

Fig. 7 Illustration of mechanism of forming GF composites by ultrasonic assisted plasma electrochemical method.

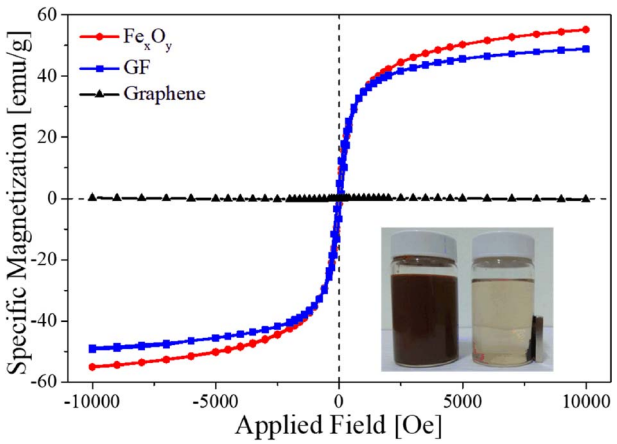

Fig. 8 The magnetization dependence of the Fe_xO_y, GF and graphene samples on the applied magnetic field at room temperature.

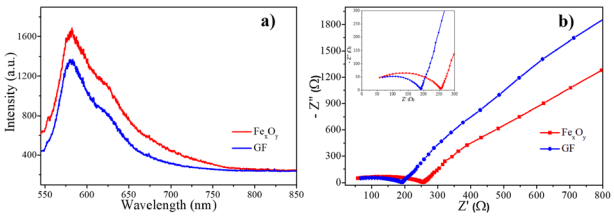

Fig. 9 (a) Photoluminescence spectroscopy (PL) and (b) electrochemical impedance spectroscopy (EIS) of Fe_xO_y and GF samples.

investigation. Fig. 9 shows the photoluminescence spectroscopy (PL) under the wavelength exciton of 325 nm and electrochemical impedance spectroscopy (EIS) of Fe_xO_y and GF samples at room temperature. PL spectrum of GF showed a similar curve as that of Fe_xO_y with the decreased peak intensity as display in Fig. 9(a). This result is related to the higher electron–hole recombination rate of Fe_xO_y than that of GF due to the interface charge transfer from Fe_xO_y to graphene. Therefore, combining iron oxide nanoparticles with graphene in an ultrasonic-assisted plasma electrochemical process prevents electron–hole pair recombination efficiently, which is beneficial to GF photocatalytic activity. EIS measurements were carried out on both Fe_xO_y and GF composite samples coat on the carbon paper substrate in the frequency range of 100 mHz to 100 kHz (Fig. 9(b)). The EIS plots of the composite GF samples have smaller arcs than the Fe_xO_y samples, which correspond to lower values of charge transfer resistance. This suggests that mixing iron oxide and graphene makes the composite material more conductive than the bare material. As a result, in the GF composite sample, the charges created during photocatalysis will be easier to separate. This result is highly agreed with the PL results above.

Fig. 10 displays the UV-vis absorption spectra of the Fe_xO_y, GF composite samples (Fig. 10(a)) and the corresponding Tauc plots for these samples (Fig. 10(b)). The GF composite sample exhibits better light absorption than the iron oxide sample with a wavelength of less than 700 nm. The band gap energies calculated for Fe_xO_y, GF samples according to the Kubelka–Munk equation are 1.65 eV and 1.76 eV, respectively. This is also shown in Fig. 10(b). These results indicate that the samples absorb light well in the visible range; the GF composite material has a synergistic effect between iron oxide and graphene, leading to better light absorption in the visible region than the iron oxide material.

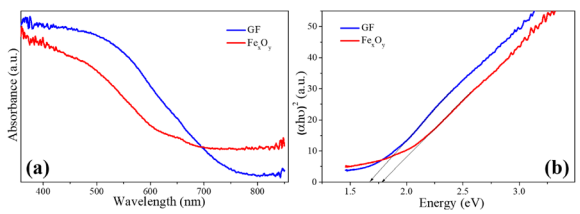

Fig. 10 (a) UV-vis absorption spectra; and (b) Tauc plots of the Fe_xO_y, GF composite samples.

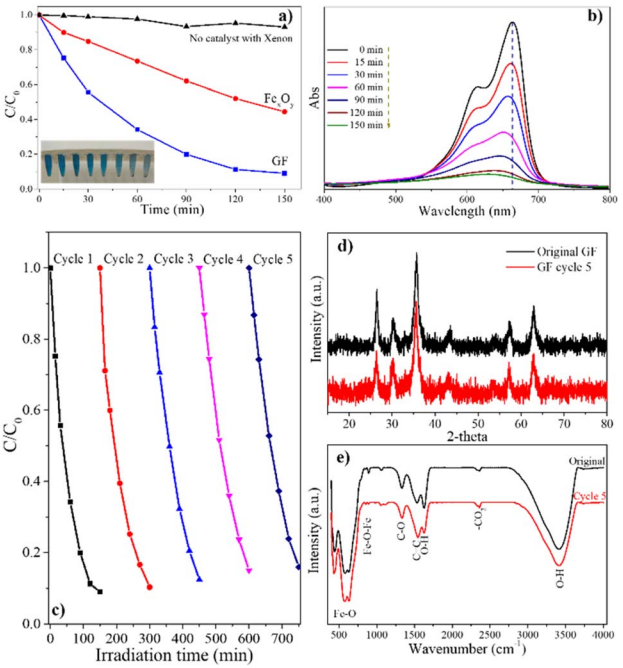

Fig. 11 (a) Compare the photocatalytic degradation of methylene blue dye with the catalysts of Fe_xO_y and GF, pH = 7; (b) the photocatalytic degradation of methylene blue dye with the catalyst GF, pH = 7; (c) five cycles of photocatalytic degradation of MB in the present of GF, (d) XRD patterns and (e) FTIR spectra of GF before and after five cycles of photodegradation of MB.

Fig. 11 depicts the photocatalytic activity of the sample as determined by MB dye degradation under the illumination of a xenon lamp for 150 minutes. Changes in the characteristic peak intensity of MB at 664 nm were used to evaluate MB efficiency degradation. Clearly, the typical peak of MB at 664 nm was dramatically decreased and slightly shifted to a small wavelength related to the progressive decomposition of MB (Fig. 11(b)). For comparison, MB photodegradation without the catalyst material was performed. Only 6.8% MB was

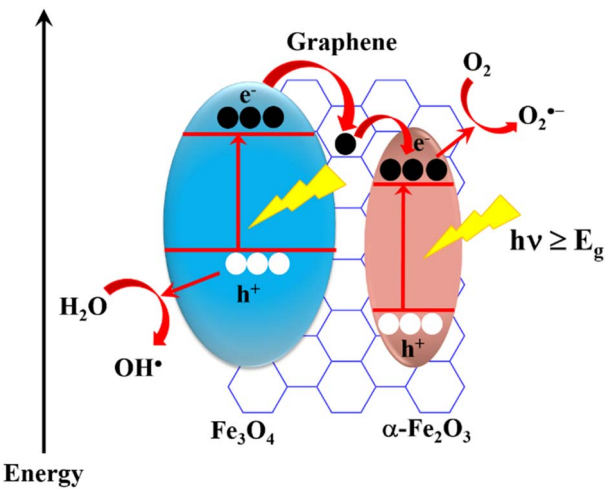

Fig. 12 Diagram of the photocatalytic degradation of MB with GF.

Table 1 The photocatalytic performance comparison with previous reports

Photocatalysts	Amount of material (mg)	Dyes	Concentration	Time (min)	Illumination power	Efficiency	Ref.
α-Fe_2O_3/graphene	30	RhB	10 mg L^{-1}	20	Xenon 350W	98%	39
α-Fe_2O_3–Fe_3O_4-M-GP	10	MO	20 mg L^{-1} (20 mL)	240	Xenon 300W	100%	40
Fe_2O_3/TiO_2	2000	MB	25 mg L^{-1} (80 mL)	300	Iodine tungsten lamp 300W	88%	41
α-Fe_2O_3/Fe_3O_4	10	CR	10 ppm (35 mL)	50	Sunlight	100%	42
rGO/Fe_3O_4	50	MB	10 ppm (50 mL)	80	Visible light lamp 400W	98.3%	43
α-Fe_2O_3	50	MB	10 ppm (100 mL)	360	UV	78%	44
γ-Fe_2O_3/GO		MB	50 ppm (50 mL)	60	Incandescent filament 60W	90.6%	45
α-Fe_2O_3/Fe_3O_4/graphene	**20**	**MB**	**20 ppm (150 mL)**	**150**	**Xenon 400W**	**91%**	**This work**

decomposed in 150 min illumination as the dark curve in Fig. 11(a). Whereas, the degradation of MB with Fe_xO_y material is 55.5%. Furthermore, the GF composite shows 1.64 times higher MB decomposite ability than that of Fe_xO_y at 91%. It is found that the graphene surface significantly increased the photocatalytic activity of Fe_xO_y. The iron oxide nanoparticles are well dispersed on the graphene surface, increasing the catalytic material's light exposure, increasing electron–hole pairing ability, and reducing recombination. More ever, the sustainability of GF was further evaluated with the solar light photocatalytic activities of samples after five cycles, revealing a slight decrease (91–84%) in the photodegradation performance (Fig. 11(c)). The effect of the Fe^{3+}/Fe^{2+} ratio was investigated using different precursor ratios of 3 : 1, 4 : 1, and 5 : 1 to prepare samples GF3, GF, and GF5, respectively. The XRD pattern of these samples exhibits a similar typical peak of graphene and Fe_3O_4 (Fig. S2†). Moreover, the photodegradation efficiency comparison of these samples shows that the optimal ratio of Fe^{3+}/Fe^{2+} is 4 : 1 as shown in Table S3.† In addition, these photocatalysts also indicate no observable changes in the XRD in FTIR spectra of the before and after the five times reused samples (Fig. 11(d and e)). In addition, the leaching of iron in the solution was estimated as shown in Tables S1 and S2.† In particular, a minor of less than 0.2% amount of iron was leached after each recovery shows the stability of graphene/Fe_xO_y composite through the photocatalyst process. These results showed that GF could be an excellent candidate for practical wastewater treatment.

From the received results, it can be seen that the photocatalytic activity of the GF composite is much larger than that of the bare Fe_xO_y. An energy band diagram was created to explain the lower rate of charge recombination in the composite materials as shown in Fig. 12. Accordingly, the E_V, E_C, and E_g energy levels generated are consistent with previous report.[38] When a suitable wavelength of light is incident on the GF material, electrons from the valence band (VB) jump to the conduction band (CB) and produce electron–hole pairs in both α-Fe_2O_3 and Fe_3O_4. Due to the difference in E_C and E_V levels of α-Fe_2O_3 and Fe_3O_4, electrons from Fe_3O_4 can direct transfer to α-Fe_2O_3 or transfer to α-Fe_2O_3 through graphene. The high electrical conductivity of graphene facilitates this process, leading electron–hole pairs to separate more easily and the charge recombination rate to decrease, then improving photocatalytic efficiency. This process is represented as follows:

$$\text{rGO/}Fe_2O_3/Fe_3O_4\ (\text{GF}) + h\nu \rightarrow (x)h^+ + (x)e^-$$

The formation of electron–hole pairs is the beginning of the photocatalytic reaction. The electrons or holes created during photocatalysis can participate in a series of subsequent reactions to form chemical radicals ($OH^{\bullet -}$, $O_2^{\bullet -}$, $HO_2^{\bullet}$, $OH^{\bullet}$, H_2O_2).[1] When chemical radicals react with MB, the decomposition products CO_2 and H_2O are produced:

$$\text{MB} + (OH^{\bullet -}, O_2^{\bullet -}, HO_2^{\bullet}, OH^{\bullet}, H_2O_2) \rightarrow CO_2 + H_2O$$

$$\text{Or MB} + \text{GF} \rightarrow \text{GF} + CO_2 + H_2O$$

Table 1 exhibits the photocatalytic performance comparison of the GFs with those of the literature reported. Compared to other leading materials, GFs show good performance.

4. Conclusion

Magnetically separable ternary graphene/α-Fe_2O_3/Fe_3O_4 visible light-driven photocatalyst (GF) was successfully synthesized through a combination of precipitation and low-temperature plasma discharge reaction. Raman, XRD, XPS and HRTEM results confirm the anchoring of iron oxide particles onto the graphene sheet. In comparison with α-Fe_2O_3 or Fe_3O_4, α-Fe_2O_3/Fe_3O_4/graphene nanocomposite exhibited better sunlight photocatalytic activity in the photodegradation of MB attributed to efficient sunlight harvesting and lower photogenerated electron–hole recombination rate. The received sunlight photocatalytic performance, efficient magnetic separation, and recyclability indicated that the as-synthesized GF could be a promising candidate for visible light driven photocatalytic application.

Conflicts of interest

There are no conflicts to declare.

Acknowledgements

This research is funded by Ministry of Natural Resources and enviroment under grant number TNMT.2022.03.14.

Notes and references

1 M. Mishra and D. M. Chun, *Appl. Catal., A*, 2015, **498**, 126–141.
2 N. J. Singh, B. Wareppam, S. Ghosh, B. P. Sahu, P. K. Ajikumar, H. P. Singh, S. Chakraborty, S. S. Pati, A. C. Oliveira, S. Barg, V. K. Garg and L. H. Singh, *Nanotechnology*, 2020, **31**, 425703.
3 S. Liu, L. Zheng, P. Yu, S. Han and X. Fang, *Adv. Funct. Mater.*, 2016, **26**, 3331–3339.
4 L. Yu, Y. Zhang, J. He, H. Zhu, X. Zhou, M. Li, Q. Yang and F. Xu, *J. Alloys Compd.*, 2018, **753**, 601–606.
5 X. Meng, Y. Xu, X. Sun, L. Xiong and Q. Wang, *J. Power Sources*, 2016, **326**, 389–396.
6 A. Kumar, P. Raizada, A. Hosseini-Bandegharaei, V. K. Thakur, V. H. Nguyen and P. Singh, *J. Mater. Chem. A*, 2021, **9**, 111–153.
7 V. Hasija, P. Raizada, A. Sudhaik, K. Sharma, A. Kumar, P. Singh, S. B. Jonnalagadda and V. K. Thakur, *Appl. Mater. Today*, 2019, **15**, 494–524.
8 J. Wang, Y. Chen, G. Liu and Y. Cao, *Composites, Part B*, 2017, **114**, 211–222.
9 Y. Miao and P. Yang, *J. Nanosci. Nanotechnol.*, 2017, **18**, 333–339.
10 B. Saiphaneendra, T. Saxena, S. A. Singh, G. Madras and C. Srivastava, *J. Environ. Chem. Eng.*, 2017, **5**, 26–37.
11 W. Wong, H. Y. Wong, A. B. M. Badruzzaman, H. H. Goh and M. Zaman, *Nanotechnology*, 2017, **28**, 042001.
12 Q. Wu, Y. Liu, H. Jing, H. Yu, Y. Lu, M. Huo and H. Huo, *Chem. Eng. J.*, 2020, **390**, 124615.
13 X. Xia, Q. Hao, W. Lei, W. Wang, D. Sun and X. Wang, *J. Mater. Chem.*, 2012, **22**, 16844–16850.
14 T. Peik-See, A. Pandikumar, L. H. Ngee, H. N. Ming and C. C. Hua, *Catal. Sci. Technol.*, 2014, **4**, 4396–4405.
15 V. Hasija, V. H. Nguyen, A. Kumar, P. Raizada, V. Krishnan, A. A. P. Khan, P. Singh, E. Lichtfouse, C. Wang and P. Thi Huong, *J. Hazard. Mater.*, 2021, **413**, 125324.
16 H. Wang, J. Shen, Y. Li, Z. Wei, G. Cao, Z. Gai, K. Hong, P. Banerjee and S. Zhou, *ACS Appl. Mater. Interfaces*, 2013, **5**, 9446–9453.
17 Y. Qin, M. Long, B. Tan and B. Zhou, *Nano-Micro Lett.*, 2014, **6**, 125–135.
18 R. Kumar, S. M. Youssry, K. Z. Ya, W. K. Tan, G. Kawamura and A. Matsuda, *Diamond Relat. Mater.*, 2020, **101**, 107622.
19 G. Williams, B. Seger and P. V. Kamat, *ACS Nano*, 2018, **2**, 1487–1491.
20 S. Banerjee, P. Benjwal, M. Singh and K. K. Kar, *Appl. Surf. Sci.*, 2018, **439**, 560–568.
21 Y. Lan, J. Deng, G. Li and Y. Luo, *J. Therm. Anal. Calorim.*, 2017, **127**, 2173–2179.
22 Z. Q. Li, H. L. Wang, L. Y. Zi, J. J. Zhang and Y. S. Zhang, *Ceram. Int.*, 2015, **41**, 10634–10643.
23 F. Wang, X. Yu, M. Ge, S. Wu, J. Guan, J. Tang, X. Wu and R. O. Ritchie, *Environ. Pollut.*, 2019, **248**, 229–237.
24 Q. Han, Z. Wang, J. Xia, S. Chen, X. Zhang and M. Ding, *Talanta*, 2012, **101**, 388–395.
25 K. Kakaei, M. D. Esrafili and A. Ehsani, *Interface Sci. Technol.*, 2019, **27**, 1–21.
26 K. Krishnamoorthy, M. Veerapandian, L. Zhang and K. Yun, *J. Phys. Chem. C*, 2012, **116**, 17280–17287.
27 D. Van Thanh, L. J. Li, C. W. Chu, P. J. Yen and K. H. Wei, *RSC Adv.*, 2014, **4**, 6946–6949.
28 Q. Chen, K. Su and M. Zhang, *J. Non-Cryst. Solids*, 2019, **511**, 166–176.
29 J. Lu, Y. Zhou, J. Lei, Z. Ao and Y. Zhou, *Chemosphere*, 2020, **251**, 126402.
30 H. Cao, R. Liang, D. Qian, J. Shao and M. Qu, *J. Phys. Chem. C*, 2011, **115**, 24688–24695.
31 S. Sagadevan, Z. Z. Chowdhury, M. R. Bin Johan, F. A. Aziz, L. S. Roselin, H. L. Hsu and R. Selvin, *Results Phys.*, 2019, **12**, 878–885.
32 M. Taraschewski, H. K. Cammenga, R. Tuckermann and S. Bauerecker, *J. Phys. Chem. A*, 2005, **109**, 3337–3343.
33 S. Guo, G. Zhang, Y. Guo and J. C. Yu, *Carbon*, 2013, **60**, 437–444.
34 J. Zhou, H. Song, L. Ma and X. Chen, *RSC Adv.*, 2011, **1**, 782–791.
35 N. A. Zubir, C. Yacou, J. Motuzas, X. Zhang and J. C. Diniz Da Costa, *Sci. Rep.*, 2014, **4**, 1–8.
36 O. Lupan, V. Postica, N. Wolff, O. Polonskyi, V. Duppel, V. Kaidas, E. Lazari, N. Ababii, F. Faupel, L. Kienle and R. Adelung, *Small*, 2017, **13**, 1–10.
37 A. S. Afify, M. Dadkhah and J. M. Tulliani, *Ceramics*, 2022, **5**, 575–592.
38 B. Lei, D. Xu, B. Wei, T. Xie, C. Xiao, W. Jin and L. Xu, *ACS Appl. Mater. Interfaces*, 2021, **13**, 4785–4795.
39 S. Han, L. Hu, Z. Liang, S. Wageh, A. A. Al-Ghamdi, Y. Chen and X. Fang, *Adv. Funct. Mater.*, 2014, **24**, 5719–5727.
40 J. Wang, Y. Chen, G. Liu and Y. Cao, *Composites, Part B*, 2017, **114**, 211–222.
41 R. Li, Y. Jia, N. Bu, J. Wu and Q. Zhen, *J. Alloys Compd.*, 2015, **643**, 88–93.
42 A. Hosseinian, H. Rezaei and A. R. Mahjoub, *Eng. Technol.*, 2011, **52**, 736–739.
43 M. Imran, M. M. Alam, S. Hussain, M. A. Ali, M. Shkir, A. Mohammad, T. Ahamad, A. Kaushik and K. Irshad, *Ceram. Int.*, 2021, **47**, 31973–31982.
44 X. H. Vu, L. H. Phuoc, N. D. Dien, T. T. H. Pham and L. D. Thanh, *J. Electron. Mater.*, 2019, **48**, 2978–2985.
45 A. Rehman, A. Daud, M. F. Warsi, I. Shakir, P. O. Agboola, M. I. Sarwar and S. Zulfiqar, *Mater. Chem. Phys.*, 2020, **256**, 123752.